



HAL
open science

Insights into the accessibility of Zr in Zr/SBA-15 mesoporous silica supports with increasing Zr loadings

Masaru Ogura, Remy Guillet-Nicolas, Dalil Brouri, Sandra Casale, Juliette Blanchard, Katie A. Cychoz, Matthias Thommes, Cyril Thomas

► To cite this version:

Masaru Ogura, Remy Guillet-Nicolas, Dalil Brouri, Sandra Casale, Juliette Blanchard, et al.. Insights into the accessibility of Zr in Zr/SBA-15 mesoporous silica supports with increasing Zr loadings. *Microporous and Mesoporous Materials*, 2016, 225, pp.440-449. 10.1016/j.micromeso.2016.01.026 . hal-01274363

HAL Id: hal-01274363

<https://hal.science/hal-01274363>

Submitted on 16 Feb 2016

HAL is a multi-disciplinary open access archive for the deposit and dissemination of scientific research documents, whether they are published or not. The documents may come from teaching and research institutions in France or abroad, or from public or private research centers.

L'archive ouverte pluridisciplinaire **HAL**, est destinée au dépôt et à la diffusion de documents scientifiques de niveau recherche, publiés ou non, émanant des établissements d'enseignement et de recherche français ou étrangers, des laboratoires publics ou privés.

Insights Into the Accessibility of Zr in Zr/SBA-15 Mesoporous Silica Supports With Increasing Zr Loadings

Masaru Ogura,¹ Remy Guillet-Nicolas,² Dalil Brouri,³ Sandra Casale,³ Juliette Blanchard,³
Katie A. Cychosz,² Matthias Thommes,² and Cyril Thomas^{3,*}

1- Institute of Industrial Science, The University of Tokyo, 4-6-1 Komaba, Meguro-ku, Tokyo
153-8505, Japan

2- Quantachrome Instruments, 1900 Corporate Drive, Boynton Beach, Florida, United States

3- Sorbonne Universités, UPMC Univ Paris 06, UMR CNRS 7197, Laboratoire de Réactivité
de Surface, 4 Place Jussieu, Tour 43-53, 3^{ème} étage, Case 178, F-75252, Paris, France

Running title: Insights Into the Accessibility of Zr Supported on SBA-15

* To whom correspondence should be addressed:

Dr. Cyril Thomas

Sorbonne Universités, UPMC Univ Paris 06, UMR 7197, Laboratoire de Réactivité de
Surface, 4 Place Jussieu, Case 178, F-75252, Paris, France

e-mail: cyril.thomas@upmc.fr

Tel: + 33 1 44 27 36 30 / Fax: + 33 1 44 27 60 33

Abstract:

Oxide-promoted SBA-15 materials have been shown to be profitable in a wide variety of catalytic reactions of environmental interest. Zr-SBA-15 materials have been found to be of particular interest in hydrotreating, biomass conversion and Fisher-Tropsch synthesis. In these studies, the accessibility of ZrO₂ located inside the silica mesoporosity has been hardly characterized, despite the fact that this may be critical in determining the best catalyst formulation. This can be accounted for by the lack of methods available for the characterization of oxides, in particular when these oxides are located in the porosity of another oxide. Recently, we have shown that ZrO₂ particles dispersed in the porosity of a SBA-15 support could be characterized via a NO_x-TPD methodology. In the present work Zr-SBA-15 materials were prepared with various loadings of Zr and thoroughly characterized through N₂-sorption coupled with advanced pore size analysis, SEM, TEM, EDS, XRD, Raman spectroscopy and NO_x-TPD. It was found that ZrO₂ accessibility decreased to a significant extent up to a Zr surface density of about 2 Zr atoms/nm² and then more slightly at higher Zr surface densities. It was also found for the first time that ZrSiO₄ was formed above 2 Zr atoms/nm². The fact that ZrSiO₄ also chemisorbed NO_x species, although to a much lower extent than ZrO₂, paves the way for a method to characterize Zr-SBA-15 samples prepared by direct synthesis for which Zr should be mainly located in the silica walls.

Keywords: NO_x-TPD; ZrO₂; ZrSiO₄; SEM; TEM

1. INTRODUCTION

Since the original discovery of the ordered mesoporous silicas (OMS) [1], these materials have been the subject of intensive investigations. Their high specific surface area together with their well-calibrated and tunable mesoporosity [1] made them attractive supports for catalysis. These mesoporous silica supports may be of particular relevance for the catalytic reactions [2,3] in which bulky molecules are involved both as reactants and products. This is typically the case for hydrotreating [4-9] and biomass conversion [10-13], for which large molecules are to be converted, and Fisher-Tropsch synthesis of long chain paraffins from syngas [14]. In these reactions, it has been reported that the introduction of ZrO₂ in the mesoporosity of OMS was extremely profitable [5,6,8-13]. One of the major concerns regarding the synthesis of oxide-loaded OMS is obviously related to the accessibility of the oxide promoter confined in the pore network of the OMS.² To the best of our knowledge and despite the significant progress that was achieved in the understanding of the porous and textural features of OMS, accessibility of Zr oxide confined in well-known SBA-15-type materials has only been scarcely addressed.

The mesopore system of SBA-15 is composed of a hexagonal arrangement of cylindrical-like mesopores surrounded by amorphous silica walls [15,16]. Depending on the details of the synthesis, SBA-15 materials may also exhibit a secondary pore system in their framework wall (i.e., intra-wall pores). These intra-wall pores are usually in the micropore to narrow mesopore range [17-19]. In ZrO₂-loaded SBA-15, accurate characterization of this complementary porosity is of particular importance as it will impact the location and the accessibility of the incorporated catalyst. As a result, chemical characterization of the confined Zr oxide species is not straightforward and only a very limited amount of techniques are available for reliable characterization. Among them, CO₂ chemisorption was reported by Garg et al. [5] on ZrO₂ dispersion in SBA-15 and the authors concluded to a decrease in its

dispersion with increasing loadings of ZrO₂. Pokrovski et al. [20] showed that CO₂ chemisorption was sensitive to the nature of the ZrO₂ polymorph. Recently, we reported that room temperature NO_x chemisorption followed by temperature-programmed desorption (NO_x-TPD) could be a promising alternative technique to assess the accessibility of ZrO₂ in SBA-15, as this technique was found to be insensitive to the ZrO₂ polymorph [21].

Considering all the above, we found it of particular interest to study the influence of Zr loading on its accessibility when supported on SBA-15 using the NO_x-TPD technique, which has been shown to provide useful characterization of various supported oxides [21-26], combined with gas physisorption, which is an important tool for the advanced analysis of complex pore structures. For that purpose, a series of Zr-SBA-15 samples was synthesized via NH₃/water vapor-induced internal hydrolysis (VIH) [27] and was thoroughly characterized through N₂-sorption, TEM-EDS, SEM, XRD, Raman spectroscopy and NO_x-TPD.

2. EXPERIMENTAL

2.1. Catalyst synthesis

The Zr-loaded samples were synthesized from two batches of SBA-15 silica supports (SBA-15-a and SBA-15-b). These SBA-15 supports were prepared following the method reported earlier by Zhao et al. [15,16]. In this method, Pluronic 123 [(EO)₂₀(PO)₇₀(EO)₂₀] (P123) non-ionic surfactant (Aldrich) was used as a structure-directing agent. The composition of the reaction mixture was 5.95 g P123/0.061 mol tetraethyl orthosilicate (tetraethoxysilane)/0.36 mol HCl/9.92 mol H₂O. The synthesized materials were filtered, washed, and dried at 100 °C overnight and then finally calcined at 500 °C under air for 6 h.

The incorporation of Zr into the SBA-15 supports was performed using ZrO(NO₃)₂·2H₂O (97 %, Wako, Japan) as a precursor. These Zr-loaded samples will be denoted as

Zr(wt%)/SBA-15-i, where i refers to as the corresponding batch of SBA-15 (a and b). The Zr precursor was wet-impregnated into the pores of SBA-15 under stirring at 60 °C until dryness and then further heated at 100 °C for 6 h in air. Depending on the targeted Zr loadings, step-wise impregnations were carried out in the Zr/SBA-15-a series. Zr(12.3)/SBA-15-a was prepared by step-wise impregnation of Zr(4.9)/SBA-15-a, whereas Zr(22.6)/SBA-15-a was prepared by step-wise impregnation of Zr(20.0)/SBA-15-a, itself issued from step-wise impregnation of Zr(9.2)/SBA-15-a. The Zr/SBA-15-b samples were also synthesized from successive Zr impregnations.

Hydrolysis of the Zr precursor (VIH method [27]) was typically carried out using a mixture of 28% NH₃ solution (5 mL) and H₂O (5 mL) placed inside a Teflon-lined 50 mL autoclave. The Zr-loaded SBA-15-i sample (0.5 g) was put in an open glass 10 mL vial and kept inside the autoclave containing the NH₃/H₂O solution without direct contact between the solid and solution. The tightly closed autoclave was then heated to 60 °C for 0.5 h. After the treatment, the solid material was dried at RT for 6 h and then at 100 °C for 12 h. The dried material was finally calcined under flowing air at 500 °C for 5 h in a muffle furnace.

2.2. Catalyst characterization

Chemical analysis of the supported catalysts was performed by inductively coupled plasma atom emission spectroscopy (ICP/AES) at the CNRS Centre of Chemical Analysis (Solaize, France).

The pore structure of the different materials was characterized by means of nitrogen at 77 K adsorption-desorption experiments using a Quantachrome Autosorb-iQ-MP gas adsorption analyzer coupled with advanced data reduction routines based on state-of-the-art non-local density functional theory (NLDFIT) [28-30]. Prior to the sorption experiments, the samples were outgassed for 12 h under turbomolecular pump vacuum (10^{-5} - 10^{-6} torr) at 423

K. Specific surface area, S_{BET} , was determined using the BET equation in the range $0.05 \leq P/P_0 \leq 0.20$ and total pore volume was obtained at $P/P_0 = 0.95$. The microporous volume and the mesoporous surface area (S_{meso}) were estimated from the t -plot (Harkin-Jura) analysis of the adsorption curve ($0.35 \text{ nm} < t < 0.65 \text{ nm}$, t being the statistical thickness).

The NO_x -temperature-programmed desorption (NO_x -TPD) experiments were carried out in a U-shape quartz reactor (15 mm i.d.). The samples were held on plugs of quartz wool, and the temperature was controlled by a Eurotherm 2408 temperature controller using a K type thermocouple. Reactant gases, used as received, were fed from independent gas cylinders (Air Liquide) by means of mass flow controllers (Brooks 5850TR) with a total flow rate of 230 $\text{mL}_{\text{NTP}}/\text{min}$. Prior to the NO_x -TPD experiments, the samples were calcined *in situ* in $\text{O}_2(20 \%) / \text{He}$ at $500 \text{ }^\circ\text{C}$ ($3 \text{ }^\circ\text{C}/\text{min}$) for 2 h with a flow rate of 100 $\text{mL}_{\text{NTP}}/\text{min}$. Typically, the composition of the adsorption mixture consisted of 400 ppm NO_x ($\sim 96 \%$ $\text{NO} + 4 \%$ NO_2) and 8 % O_2 in He. The reactor outlet was continuously monitored by a chemiluminescence NO_x analyzer (Thermo Environmental Instruments 42C-HT) that allowed the simultaneous detection of both NO and NO_2 . The samples were exposed to the adsorption mixture at RT for about 2 h until the outlet NO_x readout was equivalent to the inlet NO_x . It has been clearly demonstrated that the nature of formed ad- NO_x species was affected to a significant extent by the presence of O_2 in the NO -containing mixture [31]. As the presence of ppm levels of O_2 cannot be excluded, NO_x adsorption and desorption were carried out in the presence of a large excess of O_2 (8 %). Before the NO_x -TPD experiments, the samples were flushed in $\text{O}_2(8 \%) / \text{He}$ at RT to remove weakly chemisorbed species until the NO and NO_2 concentrations detected at the outlet were negligible. NO_x -TPD experiments were carried out from RT to $550 \text{ }^\circ\text{C}$ at a heating rate of $3 \text{ }^\circ\text{C}/\text{min}$ under a mixture of 8 % O_2 in He. As has already been reported earlier [21], it should be noted that NO_x chemisorption does not occur on SiO_2 .

Zr(4.9)/SBA-15-a and Zr(22.6)/SBA-15-a were characterized by scanning electron microscopy (SEM) at the Plate-forme of Institut des Matériaux de Paris Centre using a Hitachi (SU-70) SEM FEG ultra high resolution microscope at 5 mm working distance with a low accelerating voltage, 1kV, as the isolating materials were not metallized prior to imaging. Sample preparation consisted of depositing the powder on a carbon tape itself located on an aluminum sample holder. Images were obtained with two different detectors; an in lens secondary electrons detector (SE) for morphology studies and an in lens back-scattered electrons detector (BSE) for atomic number contrast imaging. Both signals have been mixed with a 40/60 ratio to reveal the appearance of an oxide phase different from the SBA-15 silica. The Zr/SBA-15-a series of samples was investigated by means of transmission electron microscopy (TEM). Bright field TEM and energy dispersive X-ray spectroscopy (EDS, PGT detector, EDS spot as low as 20 nm diameter) investigations were performed at the Plate-forme of Institut des Matériaux de Paris Centre using a JEOL 2010 microscope operating at 200 kV with a LaB₆ filament and equipped with an Orius CCD camera (Gatan). The powdered samples were embedded in epoxy resin and cut into thin slices (50 nm) with an ultramicrotome instrument equipped with a diamond knife.

XRD measurements were carried out using a theta-theta D8 Advance (Bruker) powder diffractometer with Cu-K α radiation (0.154 nm) operated at 30 kV and 30 mA, and equipped with a 1D LynxEye detector. The LynxEye detector was set to a 3° opening and the scanning range was 5-60° by step of 0.01°.

Raman spectra of the samples were collected from a KAISER (RXN1) Optical system equipped with a charge coupled detector (CCD) and a LASER with $\lambda = 785$ nm (power = 0.6 mW, resolution = 4 cm⁻¹, accumulation time = 10 s, 30 scans per spectrum). A microscope with an X50 long working distance (W.D. = 8.0 mm) lens was used.

3. Results

3.1. Chemical analysis and N_2 sorption

The compositions of the Zr/SBA-15-i materials are listed in Table 1. As indicated in this table, the amount of Zr introduced on the SBA-15 supports via the VIH method ranges from 4.9 to 22.6 wt%. Textural parameters of the different materials calculated from the N_2 (at 77 K) physisorption measurements are also listed in Table 1. The N_2 (at 77 K) sorption isotherms with corresponding NLDFT cumulative pore volume and pore size distribution plots obtained on the Zr/SBA-15-a series are shown in Fig. 1a-c. The samples display typical type IV isotherms with a steep capillary condensation step and the presence of a hysteresis loop, characteristic of large mesoporous-ordered SBA-15-type silicas [15-17]. Pore size analysis was first performed on the adsorption branch of the isotherms using a dedicated NLDFT method which correctly takes into account the metastabilities associated with pore condensation [28-30]. As shown in Fig. 1b, a narrow mesopore size distribution was obtained for every material, regardless of the achieved Zr loading. Although the first impregnation of the SBA-15 silica did cause a marked decrease in the mesopore mode of the material, it remains unchanged with subsequent loadings (Zr/SBA-15-a series, Fig. 1, Table 1). In contrast, the total pore volume and the BET specific surface area of the different silicas were strongly altered by increasing the amount of Zr introduced. Here it is important to note that the BET surface area values of the samples calculated from the N_2 isotherms cannot necessarily be compared in a straightforward way as they are not only affected by the amount of zirconium oxide incorporated (this will influence the accessibility of the pore network), but also depend on the quantity of silanol groups remaining on the surface. Indeed, the polarity of the adsorbent plays a major role, as it is now clearly established that it affects the orientation of the nitrogen molecule on the surface, due to its quadrupole moment. This may lead to

uncertainty regarding the cross-sectional area of the nitrogen molecule, ultimately affecting the BET surface area calculations [29]. As this latter characteristic is difficult to evaluate as a function of the loading, discussing a direct correlation between the surface area and the amount of Zr introduced is therefore difficult.

The NLDFT cumulative pore volume plots presented in Fig. 1c are of particular interest as one can clearly appreciate the noticeable pore volume associated with the intra-wall pores (between 0-6 nm) of the pristine SBA-15 material. This pore volume decreases drastically for all Zr/SBA-15 silicas which indicates that Zr species are blocking/filling this secondary porosity. As the pore size decreases with ZrO₂ introduction into the material (Table 1), ZrO₂ is coating or depositing in the main mesopores of the SBA-15 silica. To gain further insights into the location and the accessibility of the Zr species as a function of the amount introduced, the cumulative pore volume plots were recalculated considering the weight of silica only for each sample. The ZrO₂ contributes to the overall weight of the sample, but does not account for its porosity, impairing direct comparison of the pore volumes if the plots are not normalized. Normalized cumulative pore volume plots are presented in Fig. 2 for the parent SBA-15-a and three different Zr/SBA-15-a samples. One can immediately note that the small intra-wall porosity (0-4 nm) of Zr(4.9)/SBA-15-a (low loading) completely disappears, which clearly indicates that corresponding pores are no longer accessible and are filled and/or blocked by the introduction of a relatively small quantity of Zr (4.9 %). This result is in good agreement with our earlier work [21]. The cumulative pore volumes (shown up to 12 nm in Fig. 2) of the SBA-15-a sample and the one of Zr(4.9)/SBA-15-a differ by about 0.2 cm³/g. Considering that the small intra-wall porosity accounts for approximately 0.1 cm³/g (i.e., cumulative pore volume of the SBA-15-a up to 4 nm), it can be concluded that the Zr species are not only located in this secondary porosity but also dispersed on the main mesopores as already discussed above. For samples with higher Zr loadings (Zr(9.2)/SBA-15-a and

Zr(22.6)/SBA-15-a), the large intra-wall porosity is even more restricted/blocked up to about 5 nm. It is important to note that the total pore volume also progressively drops with increasing zirconia loadings which reveals that a growing amount of mesopores becomes completely inaccessible for samples containing larger amounts of Zr as compared to Zr(4.9)/SBA-15-a and SBA-15-a. This observation is consistent with the fact that oxides agglomerate at pore entrances at higher loadings as these sites provide more favorable energetic profiles. It inevitably leads to some partial or full plugging of the pores, impairing their accessibility. This result is also verified by the progressive transformation of the hysteresis loop of the Zr/SBA-15 isotherms upon loading as highlighted in Fig. 3. SBA-15a (and Zr(4.9)/SBA-15-a, see Fig 1a) exhibits a typical type H1 hysteresis loop found for well-ordered mesoporous SBA-15 silicas, where the desorption branch is not affected by any pore blocking/cavitation phenomenon and the relative pressure associated with the capillary evaporation of the adsorbate can be correlated with the width of the mesopore in a straightforward way. On the contrary, Zr(22.6)/SBA-15-a's isotherm (and Zr(20.0)/SBA-15-a, see Fig. 1a) exhibits a less steep desorption branch combined with a tailing between relative pressures of 0.6 - 0.4. The resulting hysteresis is characteristic of H2(b)/H5-type; one which describes a far more complex pore structure where network effects are of prime importance. As detailed in the recently updated IUPAC technical report on physisorption [32], these hysteresis loops are associated with delayed capillary evaporation due to the presence of smaller pore entrances (i.e., necks) as compared to the pore bodies. In Zr/SBA-15 silicas, the pore necks are resulting from the agglomeration of the ZrO₂ species at the entrance of the pores as detailed above. Depending on the degree of plugging of each mesopore, pore-blocking/percolation or cavitation induced desorption phenomena will take place, reflecting a pore structure where the size distribution of the pore neck widths is very heterogeneous and/or a pore structure containing open, partially, and fully plugged mesopores. To further evaluate

the extent of the accessibility of the pore network of Zr(22.6)/SBA-15-a (highest loading of ZrO₂), the NLDFT pore size distribution of this particular sample, calculated using the desorption branch of the corresponding isotherm, normalized to the amount of silica only was compared to its pristine SBA-15-a counterpart (Fig. 3 inset). As expected, one can clearly appreciate the three different components of the pore size distribution of Zr(22.6)/SBA-15-a. The first one (around 7.5-8 nm) corresponds to the remaining fraction of unplugged/unrestricted mesopores. The pore size associated with these freely accessible mesopores is smaller than that of the SBA-15-a, being consistent with a coating or a deposition of ZrO₂ species as relatively thin clusters on the mesopore walls. The second component corresponds to partially plugged mesopores, desorbing via a pore blocking mechanism due to the presence of pore necks. Therefore, the resulting pore size distribution from the desorption branch allows one to obtain information on the heterogeneous distribution of pore neck widths, ranging from 6 to 7 nm in this case. Finally, the last component of the pore size distribution comes from the mesopores that are heavily or fully plugged and where the neck size, if any, is below the critical one for N₂ at 77 K [33]. As a result, these pores desorb via a cavitation-controlled mechanism that generates an artificial peak at about 4-5 nm in the pore size distribution that does not represent a real population of pores [34]. This phenomenon could also be seen on the Zr/SBA-15-b series (not shown). The shape of the desorption curves differs somewhat from previously reported results [27] and can be attributed to differences in the synthesis, impregnation and/or calcination conditions. The values of the normalized surface area (NSA), a concept introduced by Landau et al. [4,35] (Table 1), also support progressive plugging of the mesopores upon introduction of Zr.

3.2. NO_x-TPD characterization

The NO_x (NO + NO₂) profiles obtained on the Zr/SBA-15-a series after exposure of the samples to a NO-O₂-He mixture at RT are shown in Fig. 4. In agreement with our earlier

study [21], these NO_x profiles show two desorption peaks at low (~ 80 °C) and high (~ 350 °C) temperatures. The reproducibility of the NO_x uptake measurements was probed on Zr(12.3)/SBA-15-a. As indicated in Table 2, both measurements were found to be in good agreement as the NO_x uptakes ($\mu\text{mol NO}_x/\text{g}$) were estimated within an accuracy of less than 5 % ($141 \pm 5 \mu\text{mol NO}_x/\text{g}$). Fig. 4 shows that the NO_x uptake increased as the amount of Zr increased in the Zr/SBA-15-a series. By considering that the NO_x surface density is $6 \mu\text{mol NO}_x / \text{m}^2_{\text{ZrO}_2}$ [22] the accessible surface of ZrO_2 can be estimated (Table 2). Fig. 5 displays the accessible surface of ZrO_2 ($\text{m}^2/\text{g}_{\text{ZrO}_2}$) as a function of the Zr surface density of the Zr/SBA-15-i materials. It can be observed that the accessible ZrO_2 surface decreases drastically as the Zr surface density increases up to about 2 Zr atoms/ nm^2 . Even if the decrease in the accessibility of ZrO_2 continues for higher Zr surface density, one can note that it is far less pronounced.

3.3. Electron microscopy characterization

3.3.1 Scanning electron microscopy (SEM)

SEM images of Zr(4.9)/SBA-15-a and Zr(22.6)/SBA-15-a are shown in Fig. 6. Z-contrast imaging was used to distinguish between silica rich and zirconia rich areas. As expected the SBA-15 consisted of bundles of cylindrical fibers (Fig. 6a-d) [36]. In the case of the Zr(4.9)/SBA-15-a sample (low Zr loading), the fiber bundles were regular (Fig. 6b) and no meaningful difference in contrast could be observed (Fig. 6c). Conversely, the highly-loaded sample (Zr(22.6)/SBA-15-a) showed fibers with a "smoother surface" (Fig. 6e) exhibiting sharp contrasts in Z-contrast imaging (Fig. 6f). The darker zones can be assigned to silica rich surfaces, whereas the lighter zones correspond to zirconia rich surfaces. This suggests that a fraction of Zr is located outside of the porosity in the highly-loaded sample as SEM

observations are solely related to the external surface of the material and oxide phases located inside the SBA-15 mesoporosity cannot be characterized.

3.3.2 Transmission electron microscopy (TEM) and EDS analyses

The TEM micrographs of selected Zr/SBA-15-a samples are shown in Fig. 7. These images show the well-known honeycomb morphology of the SBA-15 materials with well-ordered mesopores of about 7-8 nm diameter in agreement with the values calculated by N₂ sorption (Table 1). On the low-loaded sample (Zr(4.9)/SBA-15-a), no mesopore plugging could be observed (Fig 7a). In contrast, as soon as the Zr loading was higher than or equal to 9.2 wt%, mesopore plugging could be seen (Fig. 7b-d). It can also be observed that some pores contain ZrO₂, while others appear empty, in good agreement with the earlier characterization of such materials [37] and the N₂ physisorption results discussed above. High resolution images (Fig. 7e,f) indicate that the ZrO₂ particles are poorly crystalline (absence of lattice fringes) in agreement with the absence of diffraction spots (not shown). As illustrated in Fig. 7g, for which the ultrathin cut occurred parallel to the mesopores axis, the distribution of ZrO₂ inside the mesopores is rather heterogeneous, which makes the estimation of the ZrO₂ nanoparticles size and dispersion extremely challenging. In addition, dark regions located outside of the porosity could be highlighted on the samples containing Zr loadings higher than or equal to 20 wt% as illustrated in Fig. 7c-d. It was found that these dark regions were hardly crystalline as they did not lead to any diffraction spots. The Zr/Si ratios determined by EDS on various regions of the Zr/SBA-15-a series are listed in Table 3. For the samples exhibiting a Zr content lower than or equal to 12.3 wt%, the Zr/Si ratios estimated by EDS performed on the mesoporous region were found to be in agreement with those expected from chemical analysis, indicating that Zr had been effectively introduced in the SBA-15 mesoporosity. In contrast, for Zr loadings greater than or equal to 20 wt%, the Zr/Si ratios on different

mesopore regions were found to be significantly lower than those expected from chemical analysis. Let us recall that these samples also exhibited dark regions (Fig. 7c-d). EDS analysis of these particular regions led to the conclusion that the investigated compound should be enriched in Zr as the Zr/Si ratios were found to be close to unity (Table 3).

3.4. XRD

The wide angles XRD patterns obtained for the Zr/SBA-15-a samples are shown in Fig. 8a. The samples with Zr loadings lower than or equal to 12.3 wt% exhibit only a broad contribution at about 24° attributed to the amorphous silica walls [38]. For higher Zr loadings, additional contributions can be observed at 27° , 34° and 55° . These contributions cannot be attributed to the formation of ZrO_2 and will be assigned and discussed in the following paragraphs. The XRD patterns of the Zr/SBA-15-b series are compared to those of Zr(12.3)/SBA-15-a and Zr(20.0)/SBA-15-a in Fig. 8b. The Zr/SBA-15-b samples do not show the reflections observed for the highly-loaded Zr/SBA-15-a samples. For Zr(18.0)/SBA-15-b, a very weak contribution can be seen at about 30° , which could be assigned to the presence of amorphous ZrO_2 [39] in agreement with the high resolution images (Fig. 7e,f) and the absence of diffraction spots (section 3.3.2.). This difference between the two series of Zr/SBA-15 samples puts particular emphasis on the importance of the synthesis and impregnation conditions on the resulting materials.

3.5. Raman spectroscopy

Apart from contributions at 455 , 595 and 980 cm^{-1} due to the SBA-15 silica support [40], no other obvious band could be observed on the Zr/SBA-15-a series (not shown).

4. Discussion

The accessibility of Zr deposited on a SBA-15 silica support was probed by the NO_x -TPD method coupled with advanced analysis of N_2 physisorption data. It was found that the ZrO_2 accessible surface area of the Zr/SBA-15-a series decreased to a significant extent as the Zr loading increased up to 12 wt% (Fig. 5). As indicated by the N_2 sorption, especially by the changes in the hysteresis loops described earlier and TEM measurements (Table 1, Fig. 1 and Fig. 7), this decrease is essentially attributable to progressive plugging of some mesopores by ZrO_2 . A similar phenomenon has already been reported by Chandra Mouli et al. for a Zr/SBA-15 material prepared by direct synthesis, i.e. introduction of the ZrOCl_2 precursor in the course of the SBA-15 preparation [41]. EDS analyses performed on the corresponding samples showed that the Zr/Si ratios were in good agreement with those expected on the basis of chemical analysis (Table 3), indicating that Zr had been effectively introduced in the porosity of the SBA-15 silica. At higher loadings, the decrease in the accessible ZrO_2 surface (calculated assuming that Zr is exclusively present as ZrO_2) is much less pronounced than for Zr loadings lower than or equal to 12.3 wt% (Fig. 5). Combined electron microscopy investigations (SEM and TEM) revealed the presence of an additional phase located outside of the mesoporosity at such high Zr loadings (Fig. 6 f and Fig. 7c,d). In agreement with this, the Zr/Si ratios of the mesopore regions of the Zr highly-loaded samples were found to be much lower than those expected on the basis of chemical analysis (Table 3). EDS analysis of the phase located outside of the mesopores (dark regions in Fig. 7c,d) led to Zr/Si ratios of about unity (Table 3). Electron diffraction performed on these dark regions in the TEM equipment did not provide any diffraction spots indicating that this phase should be amorphous. This was also supported by the absence of Raman bands different from those attributable to the silica support on the corresponding samples. Wide angles diffraction

patterns showed broad contributions at 27, 34 and 55 ° for the Zr/SBA-15-a samples with Zr loadings higher than or equal to 20 wt% (Fig. 8a). These contributions can be attributed to the presence of a poorly crystalline zirconium silicate phase [42] (ZrSiO_4 : ICDD 00-083-1378), which fulfills the Zr/Si ratio close to unity found by EDS (Table 3). To our knowledge, the formation of ZrSiO_4 has not been reported on Zr/SBA-15 systems prepared by post-synthesis incorporation of Zr in a basic medium [5], as was the case in the present study. The formation of ZrSiO_4 has been shown to occur for a Zr/SBA-15 material prepared in a strongly acidic medium and submitted to a hydrothermal aging at 150 °C [43]. The affinity of ZrSiO_4 (ACROS, 98%, 13 m^2/g) for NO_x species (not shown) was investigated following the aforementioned described NO_x -TPD methodology. It was found that the ZrSiO_4 sample adsorbed a limited amount of NO_x species (5.6 $\mu\text{mol NO}_x/\text{g}$) resulting in a much lower NO_x surface density (0.43 $\mu\text{mol NO}_x/\text{m}^2$) compared with that found earlier for ZrO_2 (6.00 $\mu\text{mol NO}_x/\text{m}^2$ [22]). The less pronounced decrease observed in the accessible surface area of ZrO_2 for the higher Zr loading of the Zr/SBA-15-a series can thus be attributed to the formation of ZrSiO_4 and/or to the collapse of the silica mesopores making the ZrO_2 particles located inside the corresponding pores potentially more accessible.

The post-synthesis incorporation of Zr in OMS has been performed with various methods. Landau et al. showed that using chemical solution decomposition (CSD) and internal hydrolysis (IH) of $\text{Zr}(n\text{-PrO})_4$ allowed for the incorporation of significant quantities of ZrO_2 in the SBA-15 mesoporosity without pore blocking [44]. In this work the authors used non-hydrolytic sol-gel to grow ZrO_2 nanoparticles in the SBA-15 porosity without interaction with the silica walls. In contrast, pore blocking was reported when the $\text{ZrO}_2/\text{SBA-15}$ materials were prepared from SBA-15 dispersed in aqueous solutions of ZrOCl_2 by increasing the pH with NH_3OH [45]. Using the ZrOCl_2 in the presence of urea, Garg et al. did not report on mesopore blocking in the as-prepared $\text{ZrO}_2/\text{SBA-15}$ materials [5]. ZrO_2/OMS

materials were also prepared by zirconium propoxide ((Zr-PrO)₄) grafting [6,46,47]. Using an excess of Zr(*n*-PrO)₄, Gutiérrez et al. suggested that monolayer coverage of SBA-15 by ZrO₂ was reached at a Zr surface density of about 2 Zr atoms/nm² [46]. Based on Zr(IV) deposition isotherm, these authors later elegantly demonstrated that ZrO₂ monolayer on SBA-15 was reached at 2.15 Zr atoms/nm² [6]. Niu et al. reported on ZrO₂ monolayer on SBA-15 at a Zr surface density of 1.90 Zr atoms/nm² [45]. This latter value corresponded to that determined for a MCM-41 support by Wang et al. via potentiometric titration measures and the measured isoelectric points of the ZrO₂, MCM-41 and ZrO₂/MCM-41 materials [47]. All in all, these earlier studies pointed to a ZrO₂ monolayer coverage of OMS close to 2 Zr atoms/nm². On our samples, it is of interest to note that the NO_x uptake decreases much less steeply for Zr surface densities greater than about 2 Zr atoms/nm² (Fig. 5) and that ZrSiO₄ was formed above this value.

In the present work, Zr incorporation was achieved via post-synthesis of a SBA-15 silica support. Another possibility to introduce Zr consists in the use of a direct synthesis process for which the Zr precursor is added in the SBA-15 starting solution [41,48,49]. In this case, Zr should be mainly located in the silica walls of the as-synthesized Zr/SBA-15 materials and in a chemical environment close to that found in ZrSiO₄. The fact that ZrSiO₄ also chemisorbed NO_x species, although to a much lower extent than ZrO₂, thus paves the way for a method to characterize the Zr-SBA-15 samples prepared by direct synthesis.

5. Conclusions

This work reports on the characterization of accessible Zr in Zr/SBA-15 materials. For this purpose, Zr-SBA-15 materials were prepared with various loadings of Zr

and thoroughly characterized through N₂-sorption (coupled with state-of-the-art NLDFT pore structure analysis), SEM, TEM, EDS, XRD, Raman spectroscopy and NO_x-TPD. For low loadings, it was found that ZrO₂ filled/blocked the intra-wall porosity of the SBA-15 and was also deposited or coated as relatively thin clusters inside the main mesopores. With increasing Zr loadings, progressive agglomeration at pore entrances was observed, leading to partial or complete plugging of some mesopores. As a result, the ZrO₂ accessibility decreased to a significant extent up to a Zr surface density of about 2 Zr atoms/nm² and then more slightly at higher Zr surface density. It was also found for the first time that ZrSiO₄ was formed above 2 Zr atoms/nm². The fact that ZrSiO₄ also chemisorbed NO_x species, although to a much lower extent than ZrO₂, paves the way for a method to characterize Zr-SBA-15 samples prepared by direct synthesis for which Zr should be mainly located in the silica walls.

Acknowledgments

J.-M. Krafft is acknowledged for carrying out the Raman measurements. The Authors also thank O. Ben Moussa for the ZrO₂ and ZrSiO₄ XRD measurements (not shown).

References

- [1] C.T. Kresge, M.E. Leonowicz, W.J. Roth, J. Vartuli, J.S. Beck, *Nature* 359 (1992) 710-712.
- [2] F. Schüth, A. Wingen, J. Sauer, *Microporous Mesoporous Mater.* 44-45 (2001) 465-476.
- [3] E. Ghedini, M. Signirretto, F. Pinna, G. Cruciani, *Catal. Lett.* 125 (2008) 359-370.
- [4] M.V. Landau, L. Vradman, M. Herskowitz, Y. Koltypin, A. Gedanken, *J. Catal.* 201 (2001) 22-36.
- [5] S. Garg, K. Soni, G. Muthu Kumaran, M. Kumar, J.K. Gupta, L.D. Sharma, G. Murali Dhar, *Catal. Today* 130 (2008) 302-308.
- [6] O.Y. Gutiérrez, D. Valencia, G.A. Fuentes, T. Klimova, *J. Catal.* 249 (2007) 140-153.
- [7] L. Vradman, M.V. Landau, M. Herskowitz, V. Ezersky, M. Talianker, S. Nikitenko, Y. Koltypin, A. Gedanken, *J. Catal.* 213 (2003) 163-175.
- [8] O.Y. Gutiérrez, T. Klimova, *J. Catal.* 281 (2011) 50-62.
- [9] P. Biswas, P. Narayanasarma, C.M. Kotukalapudi, A.K. Dalai, J. Adjaye, *Ind. Eng. Chem. Res.* 50 (2011) 7882-7895.
- [10] X. Wang, M.V. Landau, H. Rotter, L. Vradman, A. Wolfson, A. Erenburg, *J. Catal.* 222 (2004) 565-571.
- [11] B. Katryniok, S. Paul, M. Capron, C. Lancelot, V. Bellière-Baca, P. Reye, F. Dumeignil, *Green Chem.* 12 (2010) 1922-1925.
- [12] J. Luo, J. Yu, R.J. Gorte, E. Mahmoud, D.G. Vlachos, M.A. Smith, *Catal. Sci. Technol.* 4 (2014) 3074-3081.
- [13] Y. Niu, H. Wang, X. Zhu, Z. Song, X. Xie, X. Liu, J. Han, Q. Ge, *Microporous Mesoporous Mater.* 198 (2014) 215-222.

- [14] S. Mu, D. Li, B. Hou, L. Jia, J. Chen, Y. Sun, *Energy Fuels* 24 (2010) 3715-3718.
- [15] D. Zhao, J. Feng, Q. Huo, N. Melosh, G.H. Fredrickson, B.F. Chmelka, G.D. Stucky, *Science* 279 (1998) 548-552.
- [16] D. Zhao, Q. Huo, J. Feng, B.F. Chmelka, G.D. Stucky, *J. Am. Chem. Soc.* 120 (1998) 6024-6036
- [17] M. Kruk, M. Jaroniec, C.H. Ko, R. Ryoo, *Chem. Mater.* 12 (2000) 1961-1968.
- [18] A. Galarneau, H. Cambon, F. Di Renzo, R. Ryoo, M. Choi, F. Fajula, *New J. Chem.* (27 (2003) 73-79.
- [19] R. Guillet-Nicolas, F. Bérubé, T.W. Kim, M. Thommes, *Stud. Surf. Sci. Catal.* 174 (2008) 141-148.
- [20] K. Pokrovski, K.T. Jung, A.T. Bell, *Langmuir* 17 (2001) 4297-4303.
- [21] H.Y. Law, J. Blanchard, X. Carrier, C. Thomas, *J. Phys. Chem. C* 114 (2010) 9731-9738.
- [22] C. Thomas, *J. Phys. Chem. C* 115 (2011) 2253-2256.
- [23] J. Blanchard, R.P. Doherty, H.-Y. Law, C. Méthivier, C.; Thomas, *Topics Catal.* 56 (2013) 134-139.
- [24] T. Chaieb, L. Delannoy, C. Louis, C. Thomas, *Appl. Catal. B: Environmental* 142-143 (2013) 780-784.
- [25] T. Chaieb, L. Delannoy, G. Costentin, C. Louis, S. Casale, R.L. Chantry, Z.Y. Li, C. Thomas, *Appl. Catal. B: Environmental* 156-157 (2014) 192-201.
- [26] T. Bonnotte, R.P. Doherty, C. Sayag, J.-M. Krafft, C. Méthivier, M. Sicard, F. Ser, C. Thomas, *J. Phys. Chem. C* 118 (2014) 7386-7397.
- [27] C.K. Krishnan, T. Hayashi, M. Ogura, *Adv. Mater.* 20 (2008) 2131-2136.
- [28] S.J. Gregg, K.S.W. Sing, *Adsorption, Surface Area and Porosity*, Second ed., Academic Press, New York, 1982.

- [29] F. Rouquerol, J. Rouquerol, K.S.W. Sing, P. Llewellyn, G. Maurin, Adsorption by Powders and Porous Solids, Second ed., Academic Press, Oxford, 2014.
- [30] S. Lowell, J.E. Shields, M.A. Thomas, M. Thommes, Characterization of Porous Solids and Powders: Surface Area, Pore Size and Density, First ed., Springer, Dordrecht, 2004.
- [31] O. Gorce, F. Baudin, C. Thomas, P. Da Costa, G. Djéga-Mariadassou, Appl. Catal. B: Environ. 54 (2004) 69-84.
- [32] M. Thommes, K. Kaneko, A.V. Neimark, J.P. Olivier, F. Rodriguez-Reinoso, J. Rouquerol, K.S.W. Sing, Pure Appl. Chem. 87 (2015) 1051-1069.
- [33] M. Thommes, K.A. Cychosz, Adsorption 20 (2014) 233-250.
- [34] P. Van Der Voort, P.I. Ravikovitch, K.P. De Jong, A.V. Neimark, A.H. Janssen, M. Benjelloun, E. Van Bavel, P. Cool, B.M. Weckhuysen, E.F. Vansant, Chem. Commun. 9 (2002) 1010-1011.
- [35] L. Vradman, M.V. Landau, D. Kantorovich, Y. Koltypin, A Gedanken, Microporous Mesoporous Mater. 79 (2005) 307-318.
- [36] P. Linton, J.-C. Hernandez-Garrido, P.A. Midgley, H. Wennerstrom, V. Alfredsson, Phys. Chem. Chem. Phys. 11 (2009) 10973-10982.
- [37] A.H. Janssen, C.-M. Yang, Y. Wang, F. Schüth, A.J. Koster, K. de Jong, J. Phys. Chem. B 107 (2003) 10552-10556.
- [38] L.Y. Shi, Y.M. Wang, A. Ji, L. Gao, Y. Wang, J. Mater. Chem. 15 (2005) 1392-1396.
- [39] I.-J. Kuo, N. Suzuki, Y. Yamauchi, K.C.-W. Wu, RSC Adv. 3 (2013) 2028-2034.
- [40] Y. Borodko, J.W. Ager, G.E. Marti, H. Song, K. Niesz, G.A. Somorjai, J. Phys. Chem. B 109 (2005) 17386-17390.
- [41] K. Chandra Mouli, S. Mohanty, Y. Hu, A. Dalai, J. Adjaye, Catal. Today 207 (2013) 133-144.

- [42] M.M.S. Wahsh, A.G.M. Othman, S. Abd El-Aleem, *J. Ind. Eng. Chem.* 20 (2014) 3984-3988.
- [43] S.Y. Chen, Y.-T. Chen, J.-J. Lee, S. Cheng, *Chem. Mater.* 21 (2011) 5693-5703.
- [44] M.V. Landau, L. Vradman, X. Wang, L. Titelman, *Microporous Mesoporous Mater.* 78 (2005) 117-129.
- [45] Y. Niu, H. Wang, X. Zhu, Z. Song, X. Xie, X. Liu, J. Han, Q. Ge, *Microporous Mesoporous Mater.* 198 (2014) 215-222.
- [46] O.Y. Gutiérrez, G.A. Fuentes, C. Salcedo, T Klimova, *Catal. Today* 116 (2006) 485-497.
- [47] Y. Wang, K.-Y. Lee, S. Choi, J. Liu, L.-Q. Wang, C.H.F. Peden, *Green Chem.* 9 (2007) 540-544.
- [48] V. Degirmenci, Ö.F. Erdem, A. Yilmaz, D. Michel, D. Uner, *Catal. Lett.* 115 (2007) 79-85.
- [49] W.K. Chen, H.-H. Tseng, M.C. Wei, E.-C. Su, I.-C.; Chiu, *Int. J. Hydrogen Energy* 39 (2014) 19555-19562.

Table 1. Chemical elemental analysis and N₂ sorption data.

Sample	ZrO ₂ (wt%)	S _{BET} ^(a) (m ² /g)	NSA ^(b)	Pore Volume (cm ³ /g)	Intra-walls pore vol. ^(c) (cm ³ /g)	Pore diameter ^(d) (nm)
SBA-15-a	-	809	-	1.10	0.201	7.6
SBA-15-b	-	861	-	-	-	
Zr(4.9)/SBA-15-a	6.6	536	0.71	0.82	0.094	7.3
Zr(9.2)/SBA-15-a	12.5	466	0.66	0.73	0.060	7.3
Zr(12.3)/SBA-15-a	16.7	404	0.60	0.61	0.078	7.3
Zr(12.7)/SBA-15-b	17.1	355	0.50	0.52	0.050	7.3
Zr(18.0)/SBA-15-b	24.3	531	0.81	0.69	0.149	7.3
Zr(20.0)/SBA-15-a	27.0	401	0.68	0.62	0.060	7.3
Zr(22.6)/SBA-15-a	30.5	357	0.63	0.50	0.069	7.3

^(a) BET surface area, ^(b) Normalized surface area as defined by Landau et al.^{4,35} as NSA = S_{BET} of Zr/SBA-15-i / [(100-ZrO₂ wt%)/100 * S_{BET} of the SBA-15 parent material)], ^(c) NLDFT Cumulative pore volume from 0 to 6 nm, ^(d) Pore diameter calculated from the adsorption branch of the isotherm using nonlocal density functional theory (NLDFT).

Table 2. NO_x uptake and ZrO₂ accessible surface of the studied samples deduced from the NO_x-TPD profiles shown partly in Fig. 4.

Sample	ZrO ₂ (wt%)	Zr surface density ^(a) (W/nm ²)	NO _x uptake (μmol/g)	ZrO ₂ (m ² /g)	surface (m ² /g _{ZrO2})
SBA-15-a	-	-	0	0	0
SBA-15-b	-	-	0	0	0
Zr(4.9)/SBA-15-a	6.6	0.60	112	18.6	282
Zr(9.2)/SBA-15-a	12.5	1.31	132	22.0	176
Zr(12.3)/SBA-15-a	16.7	2.02	141 ± 5	23.5±0.8	141 ± 5
Zr(12.7)/SBA-15-b	17.1	2.35	152	25.4	149
Zr(18.0)/SBA-15-b	24.3	2.24	211	35.2	145
Zr(20.0)/SBA-15-a	27.0	3.29	166	27.7	103
Zr(22.6)/SBA-15-a	30.5	4.17	200	33.4	109

^(a) calculated on the basis of the BET surface areas (Table 1) and the ZrO₂ contents of the samples.

Table 3. Zr/Si ratios determined by EDS on various regions of the Zr/SBA-15-a series of samples.

	Zr/Si at. ratio		
	Theoretical ^(a)	EDS analyses	
		Mesopores	Dark regions
Zr(4.9)/SBA-15-a	0.034	0.035±0.002	-
Zr(9.2)/SBA-15-a	0.070	0.070±0.012	-
Zr(12.3)/SBA-15-a	0.098	0.094±0.009	-
Zr(20.0)/SBA-15-a	0.180	0.069±0.012	1.11±0.10
Zr(22.6)/SBA-15-a	0.214	0.102±0.026	1.06±0.02

^(a) based on the ZrO₂ contents listed in Table 1.

Figure Captions

Fig. 1. N₂ at 77K adsorption-desorption isotherms measured on the Zr-SBA-15-a series (a) with corresponding NLDFT pore size distributions (b) and cumulative pore volume plots (c). (For interpretation of references to color in this figure legend, the reader is referred to the web version of the article).

Fig. 2. NLDFT cumulative pore volume plots N₂ (77 K) normalized by the amount of silica only obtained for SBA-15-a, Zr(4.9)/SBA-15-a, Zr(9.2)/SBA-15-a and Zr(22.6)/SBA-15-a (For interpretation of references to color in this figure legend, the reader is referred to the web version of the article).

Fig 3. N₂ at 77 K adsorption-desorption normalized isotherms measured on SBA-15-a and Zr(22.6)/SBA-15-a. NLDFT pore size distributions obtained from the desorption branch for both materials are presented in the inset (For interpretation of references to color in this figure legend, the reader is referred to the web version of the article).

Fig. 4. NO_x-TPD profiles measured in O₂-He (8% in He) on the Zr/SBA-15-a series after exposure of the samples to NO-O₂-He (400 ppm-8%-balance) at RT. (For interpretation of references to color in this figure legend, the reader is referred to the web version of the article).

Fig. 5. Accessible surface of ZrO₂ estimated from the NO_x uptakes obtained from the NO_x-TPD profiles shown partly in Fig. 4. ● Zr/SBA-15-a series, ○ Zr/SBA-15-b series.

Fig. 6. SEM images of Zr(4.9)/SBA-15 (a,b: morphology and c: Z-contrast imaging) and Zr(22.6)/SBA-15 (d,e: morphology and f: Z-contrast imaging).

Fig. 7. TEM images of (a) Zr(4.9)-SBA-15-a, (b,g) Zr(9.2)-SBA-15-a, (c) Zr(20.0)-SBA-15-a and (d) Zr(22.6)-SBA-15-a, and HRTEM images of (e,f) Zr(9.2)-SBA-15-a. The scale bar is 100 nm in (a-d) and (g), 10 nm in (e) and 2 nm in (f).

Fig. 8. Wide angles XRD patterns of (a) the Zr/SBA-15-a samples and (b) the Zr/SBA-15-b samples compared to those of Zr(12.3)/SBA-15-a and Zr(20.0)/SBA-15-a. (For interpretation of references to color in this figure legend, the reader is referred to the web version of the article).

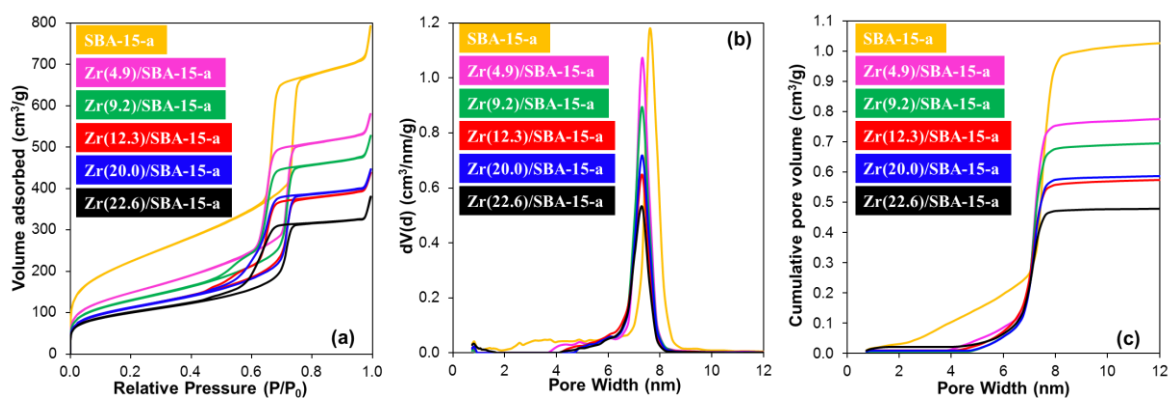


Fig. 1. N₂ at 77K adsorption-desorption isotherms measured on the Zr-SBA-15-a series (a) with corresponding NLDFT pore size distributions (b) and cumulative pore volume plots (c). (For interpretation of references to color in this figure legend, the reader is referred to the web version of the article).

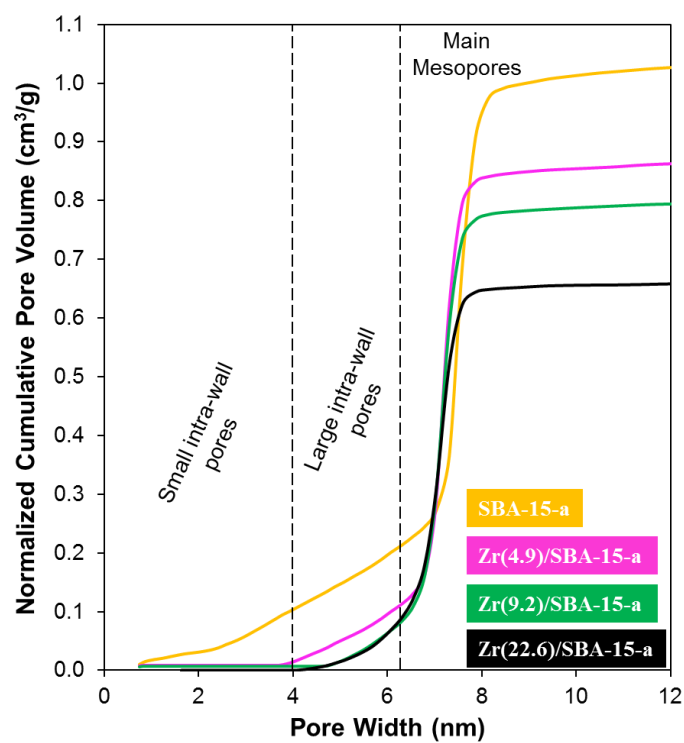


Fig. 2. NLDFT cumulative pore volume plots N_2 (77 K) normalized by the amount of silica only obtained for SBA-15-a, Zr(4.9)/SBA-15-a, Zr(9.2)/SBA-15-a and Zr(22.6)/SBA-15-a (For interpretation of references to color in this figure legend, the reader is referred to the web version of the article).

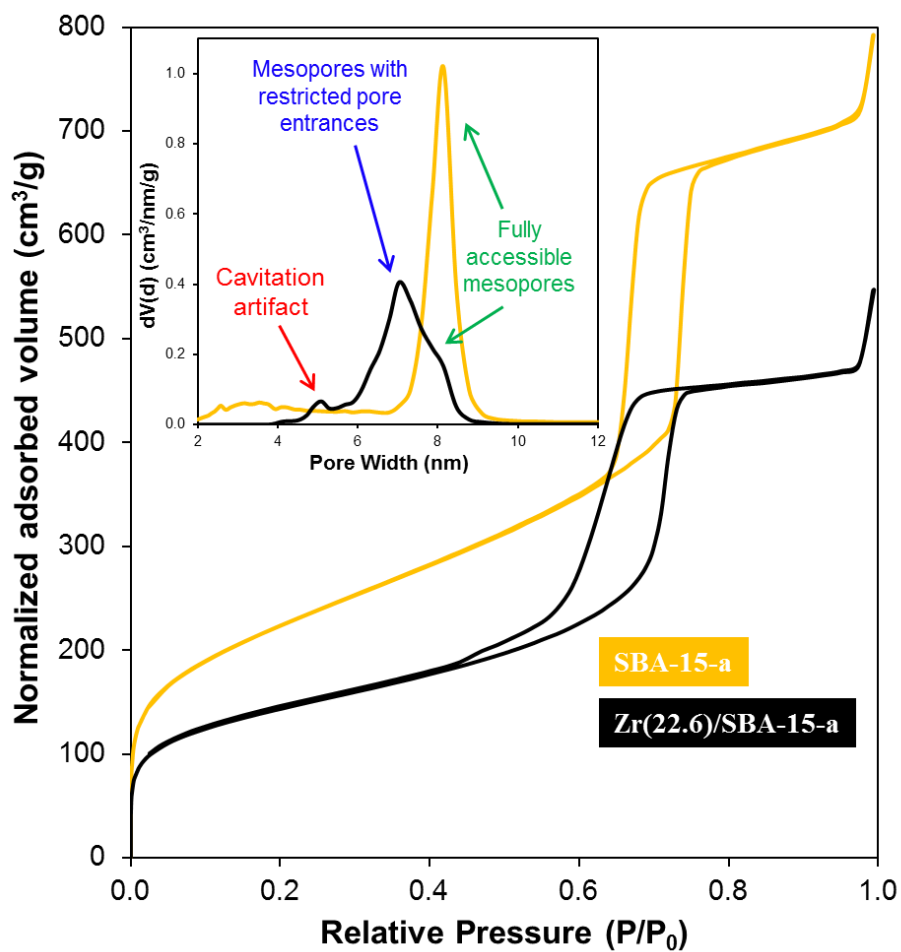


Fig 3. N₂ at 77 K adsorption-desorption normalized isotherms measured on SBA-15-a and Zr(22.6)/SBA-15-a. NLDFT pore size distributions obtained from the desorption branch for both materials are presented in the inset (For interpretation of references to color in this figure legend, the reader is referred to the web version of the article).

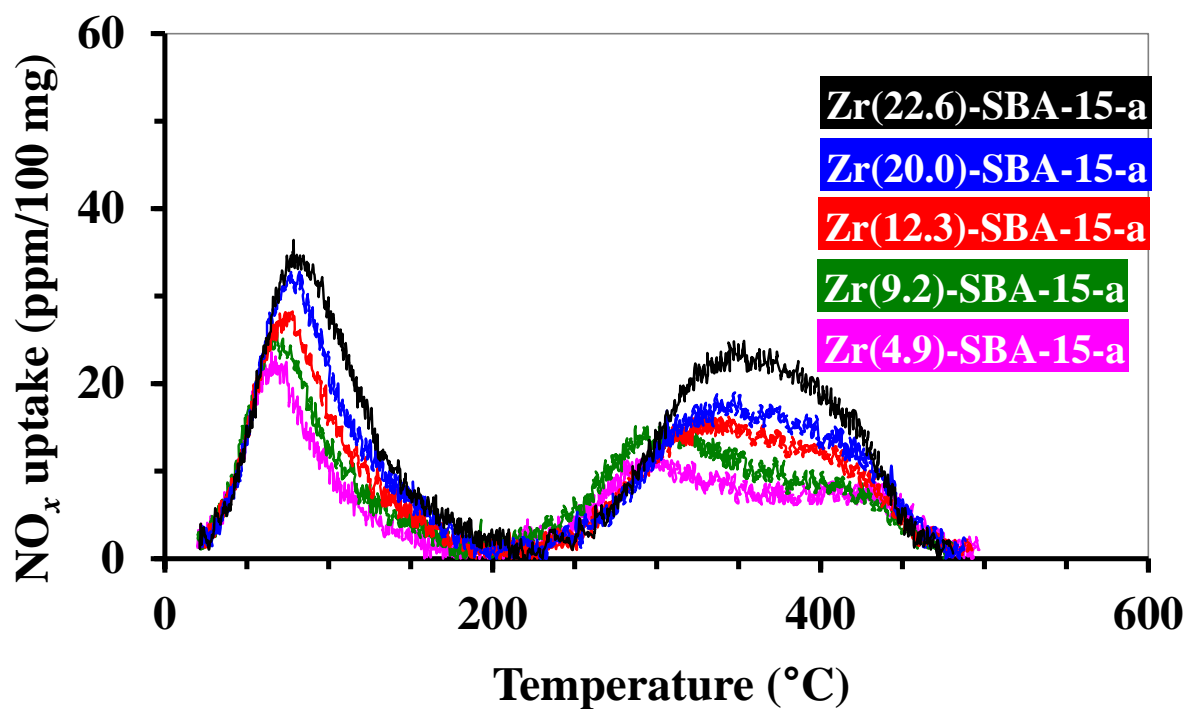


Fig. 4. NO_x-TPD profiles measured in O₂-He (8% in He) on the Zr/SBA-15-a series after exposure of the samples to NO-O₂-He (400 ppm-8%-balance) at RT. (For interpretation of references to color in this figure legend, the reader is referred to the web version of the article).

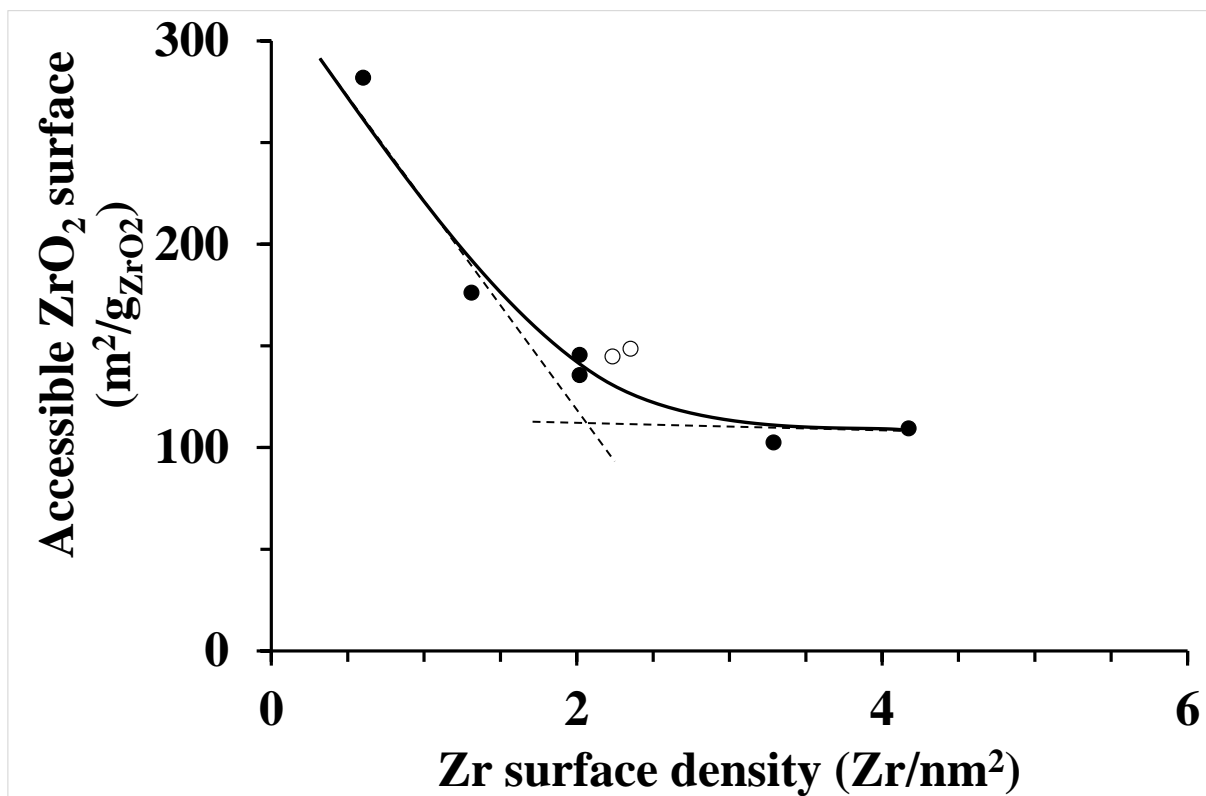


Fig. 5. Accessible surface of ZrO₂ estimated from the NO_x uptakes obtained from the NO_x-TPD profiles shown partly in Fig. 4. ● Zr/SBA-15-a series, ○ Zr/SBA-15-b series.

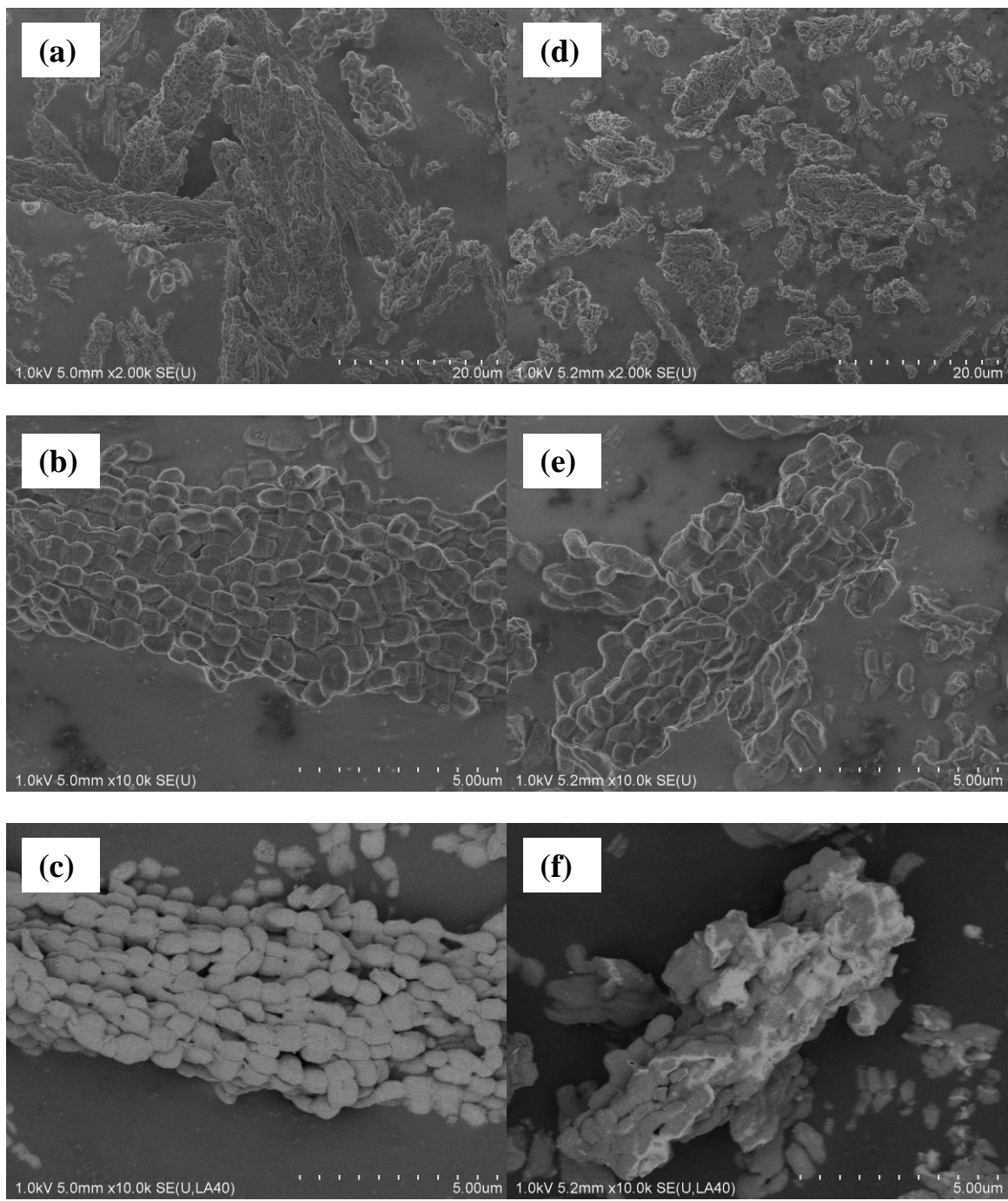


Fig. 6. SEM images of Zr(4.9)/SBA-15 (a,b: morphology and c: Z-contrast imaging) and Zr(22.6)/SBA-15 (d,e: morphology and f: Z-contrast imaging).

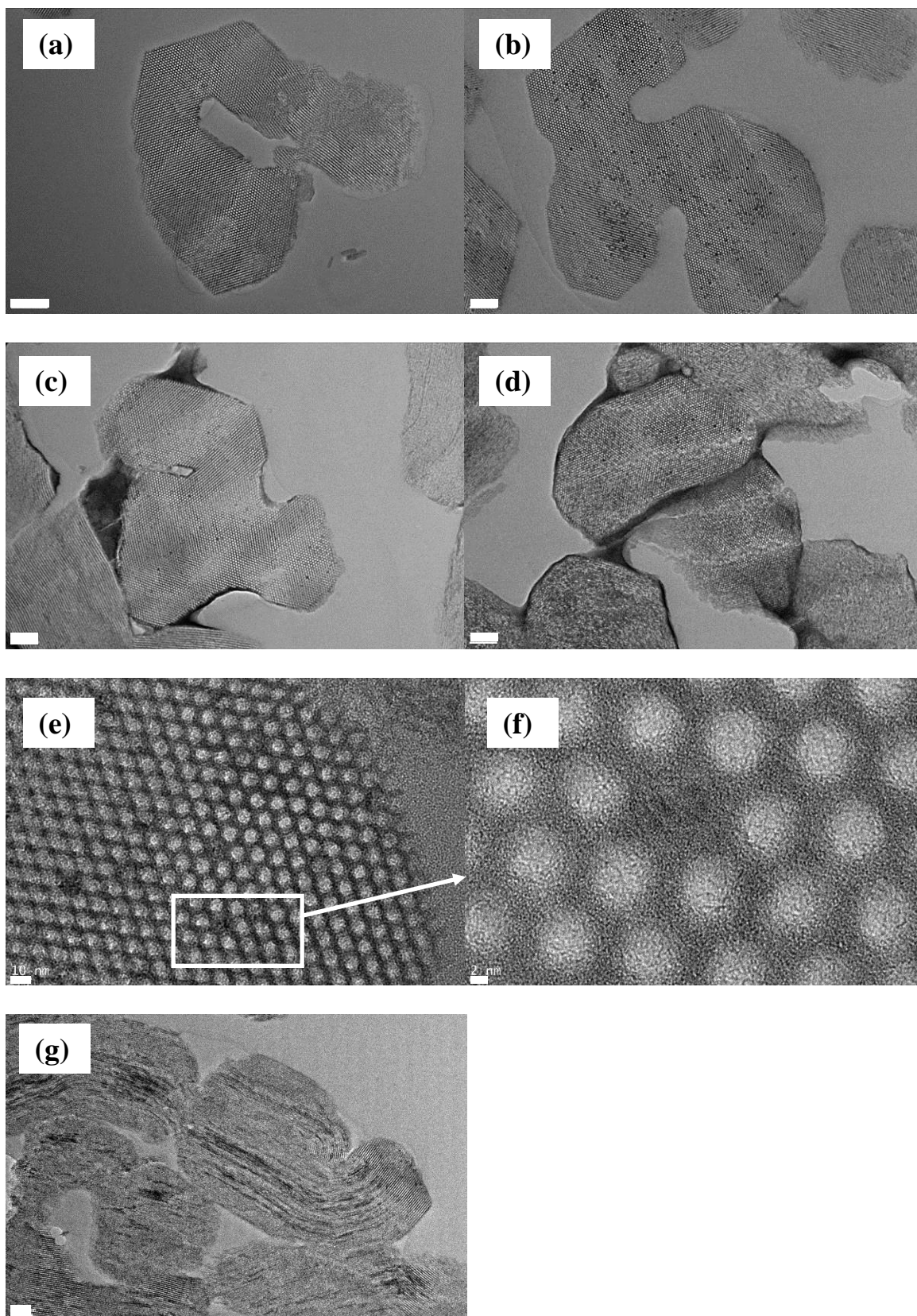


Fig. 7.

Fig. 7. TEM images of (a) Zr(4.9)-SBA-15-a, (b,g) Zr(9.2)-SBA-15-a, (c) Zr(20.0)-SBA-15-a and (d) Zr(22.6)-SBA-15-a, and HRTEM images of (e,f) Zr(9.2)-SBA-15-a. The scale bar is 100 nm in (a-d) and (g), 10 nm in (e) and 2 nm in (f).

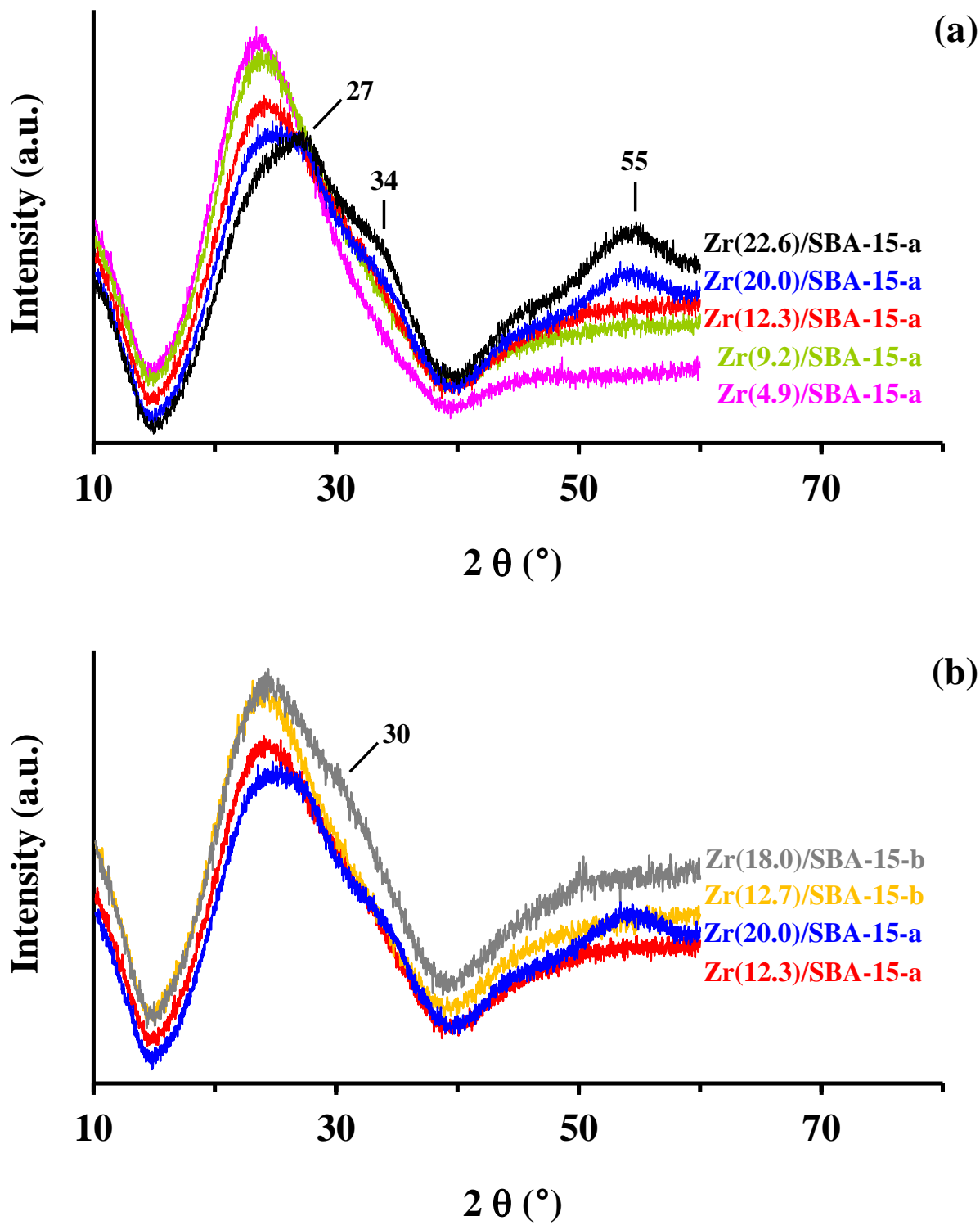


Fig. 8. Wide angles XRD patterns of (a) the Zr/SBA-15-a samples and (b) the Zr/SBA-15-b samples compared to those of Zr(12.3)/SBA-15-a and Zr(20.0)/SBA-15-a. (For interpretation of references to color in this figure legend, the reader is referred to the web version of the article).